Tungsten and molybdenum isotopic evidence for an impact origin of pallasites

Thomas S. Kruijer [a,*], Christoph Burkhardt [b], Lars E. Borg [a], Thorsten Kleine [b,c]

[a] *Nuclear and Chemical Sciences Division, Lawrence Livermore National Laboratory, 7000 East Avenue (L-231), Livermore, CA 94550, USA*
[b] *Institut für Planetologie, University of Münster, Wilhelm-Klemm-Strasse 10, 48149, Münster, Germany*
[c] *Max Planck Institute for Solar System Research, Justus-von-Liebig-Weg 3, 37077 Göttingen, Germany*

ARTICLE INFO

ABSTRACT

The origin of pallasites—stony-iron meteorites mainly composed of olivine and Fe-Ni metal—is debated and proposed formation scenarios broadly range from models that explain pallasite formation by internal processes in the mantle of a differentiated planetesimal to those that involve impact–induced mixing of core and mantle materials. Here, the origin of pallasites is examined by studying the nebular source regions of their precursor material using Mo isotopes and their history of metal-silicate segregation using Hf-W chronometry. We report new Mo and W isotopic data for a large suite of pallasite metal samples, alongside Pt isotope data to quantify superimposed cosmic ray exposure effects. Most main-group pallasites exhibit uniform pre-exposure ^{182}W and Mo isotopic compositions that bear an excellent similarity to those of IIIAB iron meteorites. Four main-group pallasites and the IIIAB iron Thunda have more radiogenic pre-exposure ^{182}W compositions, but display the same Mo isotopic composition as other main-group pallasites and IIIAB irons. This strong chronological and genetic link strongly suggests that main-group pallasite metal originated in the IIIAB parent body core. This, combined with prior Pd-Ag chronometric evidence for an early collisional disruption of the IIIAB parent body, implies that main-group pallasites formed by impact–induced mixing of metal and silicates rather than by an internal process on the IIIAB parent body. This mixing led to elevated ^{182}W compositions in some pallasites, which are best accounted for by partial re-equilibration of IIIAB metal with radiogenic ^{182}W from the colliding body. Collectively, our results support models that explain main-group pallasite formation by injection of pallasite metal into the mantle of another differentiated body, implying that pallasite silicates did not primarily derive from the IIIAB mantle, but instead from that of the colliding body.

© 2022 Elsevier B.V. All rights reserved.

1. Introduction

Differentiated meteorites derive from some of the oldest planetesimals of the Solar System and determining the timescales and processes of their formation is, therefore, crucial for understanding the Solar System's early history. There is consensus that most iron meteorites represent material from the metallic cores of planetesimals, whereas basaltic achondrites derive from the mantle and crust of such objects. However, the origin of pallasites—stony–iron meteorites composed of olivine and accessory phases embedded in an Fe-Ni metal matrix—is less clear. Although there is general agreement that pallasites are mixtures of mantle- and core-derived material (Benedix et al., 2014), the exact mechanism of their formation remains debated (Boesenberg et al., 2012). Proposed forma-

tion scenarios include derivation from the core–mantle boundary of a differentiated object (Wood, 1978; Wasson and Choi, 2003), mixing during planetesimal collisions (e.g., Tarduno et al., 2012; Walte et al., 2020), and ferrovolcanism (e.g., Johnson et al., 2020; Tarduno et al., 2012; Walte et al., 2020).

Oxygen isotope analyses of pallasite olivines reveals that most pallasites (>90%) share a common O isotopic composition (Clayton and Mayeda, 1996; Greenwood et al., 2015). They constitute the main group (MG) and are thought to originate from a single parent body. By contrast, several minor pallasite groups, such as the Eagle Station pallasites (PES) as well as several ungrouped pallasites, exhibit distinct O isotopic compositions, indicating derivation from several other parent bodies. Traditionally, MG pallasites have been viewed as samples that formed close to the core-mantle boundary of a differentiated planetesimal (Wood, 1978). This model is supported by chemical evidence suggesting that MG pallasites represent late-stage liquids of the IIIAB core (Wasson and Choi, 2003), and by broadly similar isotopic signatures of MG pallasites and

IIIAB irons (Burkhardt et al., 2011; Clayton and Mayeda, 1996; Dottin et al., 2018; Greenwood et al., 2015). However, this formation model has been disputed on the basis of, among other arguments, the strongly dissimilar cooling rates of IIIAB iron meteorites and pallasites (Yang and Goldstein, 2006; Yang et al., 2010), which are difficult to reconcile with an origin of MG pallasites near the core-mantle boundary of the IIIAB iron meteorite parent body. Instead, it has been proposed that MG pallasites are impact-generated mixtures of core and mantle material (Scott, 1977; Tarduno et al., 2012; Yang et al., 2010). These impact-related models differ in the source of pallasite silicate and metal and whether they derive from the core and mantle of a single body or distinct bodies. For instance, Yang et al. (2010) proposed that pallasites formed by re-accretion of excavated molten core and mantle material from a single differentiated planetesimal that had been disrupted during the collision with a larger body. By contrast, Tarduno et al. (2012) argued that MG pallasites formed by injection of liquid Fe-Ni metal from the core of an impactor into the mantle of another body. More recently, Walte et al. (2020), on the basis of high temperature deformation experiments, proposed a hybrid model where pallasites formed by a combination of inefficient core formation and metal injection during impact. Finally, Johnson et al. (2020) argued that pallasites formed by a process called ferrovolcanism, where late-stage core liquids buoyantly rise through the overlying mantle (Abrahams and Nimmo, 2019) producing mixtures of olivine and Fe-Ni metal from the same parent body. Distinguishing between these models of pallasite formation requires a re-evaluation of whether MG pallasite metal and IIIAB iron meteorites are genetically linked, and whether such a putative link can be reconciled with an internal or an impact-related origin of pallasites.

Molybdenum isotopes are ideal tracers for determining whether MG pallasite metal is genetically linked to IIIAB iron meteorites. This is because there are widespread nucleosynthetic Mo isotope anomalies among meteorites (Burkhardt et al., 2011) and because Mo isotopes allow distinguishing between non-carbonaceous (NC) and carbonaceous (CC) meteorites, which probably represent material from the inner and outer solar system (e.g., Budde et al., 2016; Kruijer et al., 2020; Warren, 2011). Until now only four pallasites have been analyzed for Mo isotopes, namely Eagle Station and Milton, which belong to the CC meteorites, and two MG pallasites (Brenham, Imilac) (Burkhardt et al., 2011; Dauphas et al., 2002; Hilton et al., 2019). Although the Mo isotopic composition of the latter two samples is broadly consistent with that of IIIAB irons, the data for only two samples preclude a thorough assessment of whether IIIAB iron meteorites and MG pallasites are genetically related.

A potential link between MG pallasite metal and IIIAB iron meteorites may also be evaluated using the short-lived ^{182}Hf-^{182}W system. This chronometer is ideally suited for studying the timescales and processes of metal-silicate separation on meteorite parent bodies (Kleine and Walker, 2017). The Hf-W system, therefore, allows assessing whether MG pallasite metal and IIIAB irons are chronologically linked, as would be expected for derivation from a common precursor body. Previous Hf-W studies of pallasites showed that MG pallasites exhibit large and variable deficits in ^{182}W (Quitté et al., 2005), similar to those observed for iron meteorites. However, the precision of the ^{182}W measurements achievable at the time of these studies was considerably lower than at present. Moreover, cosmic ray exposure (CRE) may have modified the W isotopic compositions of pallasites (Kruijer et al., 2013, 2012). Since prior W isotope studies on pallasites did not quantify these effects, these data are unsuitable for evaluating any potential chronological link between MG pallasite metal and IIIAB iron meteorites.

We obtained high-precision W and Mo isotopic data for a comprehensive suite of pallasites. For the same samples we also determined Pt isotopic compositions, to quantify any CRE-induced neutron capture effects on W and Mo isotopes. The combined Mo and W isotope results provide new constraints on the nebular heritage and formation timescales of pallasites and in particular on the relationship between MG pallasites and IIIAB irons, which in turn are used to derive a formation model for MG pallasites.

2. Analytical methods

2.1. Sample preparation and chemical separation

Eighteen pallasite metal samples from 15 individual MG pallasites, one ungrouped pallasite (Vermillion), and Eagle Station (PES) were selected for this study (Tables 1–3). In addition, we report Pt and W isotopic data for the IIIAB iron Thunda, which supplement the existing dataset for IIIAB iron meteorites (Kruijer et al., 2014b). Metal samples (∼0.5-1 g) were separated from the bulk pallasite samples using a diamond saw and by gentle crushing in an agate mortar. Subsequently, the metal samples were polished with abrasives (SiC), and ultrasonically cleaned in ethanol to remove any saw marks and adhering dust. To remove any terrestrial contamination and/or remaining silicates, pallasite metal samples were leached in 6 M HCl–1 M HF mixtures on a hotplate for 10-15 minutes. The metal samples were digested in 20-40 mL concentrated HNO_3–HCl (2:1) on a hotplate (120-130 °C) for at least 24 h. After complete digestion, aliquots were taken from the sample solutions for separation of Pt (∼10%), and W and Mo (∼90%).

The chemical purification of Pt followed the techniques described in our prior work (Kruijer et al., 2013, 2014b). Tungsten and Mo were separated from the sample matrix using a primary anion chromatography step using 4 mL anion exchange resin (Biorad AG1×8, 200-400 mesh). The W cuts from the first column were further purified using a cleanup anion chromatography step as described in detail elsewhere (Kleine et al., 2012; Kruijer and Kleine, 2018). The Mo cuts from the W chemistry were further purified from remaining Fe, Ru, and Zr in an additional anion exchange step (2 mL Biorad AG1×8, 100-200 mesh) and two passes over cation exchange columns (1 mL Eichrom TRU resin) (Burkhardt et al., 2011). Total procedural yields after the chemical separation were 60-80% for Pt, 70-100% for W, and 80-100% for Mo. Total procedural blanks were <100 pg for Pt, <150 pg for W, and <2 ng for Mo, which were inconsequential given the large amounts of each element analyzed (∼20-150 ng W, ∼50-500 ng Pt, and ∼1000-8000 ng Mo).

2.2. Mass spectrometry

The isotope compositions were measured on a ThermoScientific Neptune *Plus* MC-ICPMS at the University of Münster (Pt, W and Mo) and at Lawrence Livermore National Laboratory (W) using our previously established procedures (Budde et al., 2019; Kruijer et al., 2017; Kruijer and Kleine, 2018). In brief, for all three elements, the sample solutions were introduced into the mass spectrometer using self-aspirating ESI or Savillex C-Flow PFA nebulizers (∼50 µl/min. uptake rate) that were connected to a Teledyne CETAC Aridus II desolvating system. For Pt, the measurements were performed using standard Ni sampler and skimmer cones. Total ion beam intensities of 3.5×10^{-10} A were obtained for 250 ppb Pt standard solutions at an uptake rate of ∼50 µL/min. Each Pt isotope measurement consisted of a 60 s electronic baseline measurement followed by 100 isotope ratio measurements of 4.2 s integration time each. Instrumental mass bias was corrected by internal normalization to either ^{196}Pt/^{195}Pt = 0.7464 (denoted '6/5')

Table 1

Platinum isotopic compositions of pallasites and iron meteorites.

Meteorite	Collection ID	ID	N^a	Normalized to ^{196}Pt/^{195}Pt			Normalized to ^{198}Pt/^{195}Pt			
				ε^{192}Pt $(\pm2\sigma)^b$	ε^{194}Pt $(\pm2\sigma)^b$	ε^{198}Pt $(\pm2\sigma)^b$	ε^{192}Pt $(\pm2\sigma)^b$	ε^{194}Pt $(\pm2\sigma)^b$	ε^{196}Pt $(\pm2\sigma)^b$	ε^{196}Pt $(\pm2\sigma)_{\text{corr.}}^c$
Main-group (MG) pallasites										
Acomita	ME 3382	DG05	1	0.18 ± 1.46	0.32 ± 0.15	-0.35 ± 0.22	-0.29 ± 1.35	0.14 ± 0.10	0.12 ± 0.07	0.18 ± 0.07
Admire	USNM 703	DE07	1	0.63 ± 1.46	0.19 ± 0.15	0.02 ± 0.22	0.54 ± 1.35	0.18 ± 0.10	-0.01 ± 0.07	0.05 ± 0.07
Ahumada	ME 780 #30	DE06	1	2.76 ± 1.46	0.36 ± 0.15	-0.76 ± 0.22	2.76 ± 1.35	0.12 ± 0.10	0.26 ± 0.07	0.32 ± 0.07
Brenham	ME1272 #3	DE01	2	-1.51 ± 1.46	-0.03 ± 0.15	0.04 ± 0.22	-1.53 ± 1.35	0.02 ± 0.10	-0.01 ± 0.07	0.05 ± 0.07
Giroux	USNM 1574	DE08	1	-0.65 ± 1.46	0.17 ± 0.15	0.00 ± 0.22	-0.56 ± 1.35	0.18 ± 0.10	0.00 ± 0.07	0.06 ± 0.07
Huckitta	USNM 6857	DG01	2	6.43 ± 1.46	0.66 ± 0.15	-1.00 ± 0.22	5.54 ± 1.35	0.35 ± 0.10	0.34 ± 0.07	0.40 ± 0.07
Imilac	ME 1267 #14	DE02	1	3.98 ± 1.46	0.55 ± 0.15	-0.81 ± 0.22	3.98 ± 1.35	0.25 ± 0.10	0.27 ± 0.07	0.33 ± 0.07
Imilac	USNM 2180	DG07	1	3.28 ± 1.98	0.53 ± 0.30	-0.57 ± 0.30	2.70 ± 1.80	0.34 ± 0.26	0.19 ± 0.10	0.25 ± 0.10
Krasnojarsk	LLNL	DB03	1	1.41 ± 1.46	0.48 ± 0.15	-0.29 ± 0.22	1.09 ± 1.35	0.30 ± 0.10	0.10 ± 0.07	0.16 ± 0.07
Marjalahti	BM.1920,318	DG04	1	2.12 ± 1.46	0.24 ± 0.15	-0.13 ± 0.22	1.81 ± 1.35	0.18 ± 0.10	0.04 ± 0.07	0.10 ± 0.07
Mount Vernon	USNM 300	DG09	1	-0.35 ± 1.46	0.08 ± 0.15	-0.03 ± 0.22	-0.46 ± 1.35	0.07 ± 0.10	0.01 ± 0.07	0.07 ± 0.07
Newport	USNM 847	DG03	1	-0.40 ± 1.98	0.30 ± 0.30	-0.26 ± 0.30	-0.66 ± 1.80	0.20 ± 0.26	0.09 ± 0.10	0.15 ± 0.10
Pavlodar	LLNL	DB04	5	7.84 ± 0.62	0.41 ± 0.07	-0.33 ± 0.12	7.53 ± 0.76	0.30 ± 0.06	0.11 ± 0.04	0.17 ± 0.04
South Bend	ME 607 #14	DG02	1	2.07 ± 1.46	0.31 ± 0.15	-0.45 ± 0.22	1.61 ± 1.35	0.12 ± 0.10	0.15 ± 0.07	0.21 ± 0.07
Springwater	USNM 7816	DE05	1	2.74 ± 1.46	0.55 ± 0.15	-0.70 ± 0.22	1.84 ± 1.35	0.27 ± 0.10	0.23 ± 0.07	0.29 ± 0.07
Thiel Mountains	USNM 2180	DG06	1	1.93 ± 1.46	0.38 ± 0.15	-0.37 ± 0.22	1.54 ± 1.35	0.22 ± 0.10	0.12 ± 0.07	0.18 ± 0.07
Ungrouped pallasites										
Vermillion	USNM 6851	DE03	1	22.83 ± 1.46	1.37 ± 0.15	-1.90 ± 0.22	22.83 ± 1.35	0.74 ± 0.10	0.63 ± 0.07	0.69 ± 0.07
Eagle Station (PES) pallasites										
Eagle Station	ME180#5	DK02	5	-0.89 ± 0.64	-0.04 ± 0.07	0.05 ± 0.16	-0.88 ± 0.74	-0.02 ± 0.07	-0.02 ± 0.05	0.04 ± 0.05
IIIAB iron meteorites										
Thunda	Münster	Z02	2	0.37 ± 1.30	0.19 ± 0.12	-0.27 ± 0.21	0.14 ± 1.30	0.10 ± 0.10	0.09 ± 0.07	0.15 ± 0.07
Thunda (Replicate)	Münster	AG02	3	0.61 ± 1.70	0.12 ± 0.12	-0.21 ± 0.21	0.39 ± 1.90	0.06 ± 0.11	0.07 ± 0.07	0.13 ± 0.07
Thunda (Weighted mean, $N = 2$)				0.50 ± 1.08	0.17 ± 0.09	-0.24 ± 0.15	0.31 ± 1.32	0.09 ± 0.08	0.08 ± 0.05	0.14 ± 0.05

^{a} N = Number of solution replicate analyses. One single analysis comprises 100 isotope ratio measurements of 4.2 s integration time each.

^{b} Platinum isotopic ratios are normalized to either ^{198}Pt/^{195}Pt = 0.2145 or ^{196}Pt/^{195}Pt = 0.7464 using the exponential law. The uncertainties reported for measured ε^iPt values of samples represent the 2s.d. obtained from repeated analyses of the terrestrial standard NIST129c (Table S1 and Kruijer et al., 2017) in case $N < 4$ or in the case $N > 4$, the 95% conf. limits of the mean [i.e., according to (s.d. $\times t_{0.95,N-1})/\sqrt{N}$]. However, in the case that the standard error (2s.e.) based on internal run statistics of an individual sample exceeded the long-term reproducibility (2s.d.) of NIST129c, then the former (i.e., the 2s.e. uncertainties) are reported instead.

^{c} ε^{196}Pt $(\pm2\sigma)_{\text{corr.}}$: ε^{196}Pt $(\pm2\sigma)_{\text{meas.}}$ renormalized to the pre-exposure ε^{196}Pt of -0.06 ± 0.01 (Spitzer et al., 2021).

or ^{198}Pt/^{195}Pt = 0.2145 (denoted '8/5') using the exponential law. For W, the measurements were performed using high-sensitivity Jet sampler and X skimmer cones. Total ion beams of 2.8-3.2 $\times$ 10^{-10} A were obtained for 40 ppb W standard solutions at an uptake rate of ~50 μL/min. A single W isotope measurement comprised a 60 s electronic baseline measurement followed by 200 isotope ratio measurements of 4.2 s integration time each. Instrumental mass bias was corrected by internal normalization to either ^{186}W/^{183}W = 1.9859 (denoted '6/3') or ^{186}W/^{184}W = 0.92767 (denoted '6/4'), using the exponential law. The Mo isotope analyses were performed using standard Ni sampler and (H) skimmer cones. Total ion beams of 1.2 $\times$ 10^{-10} were obtained for ~100 ppb Mo standard solutions at an uptake rate of ~50 μL/min. Each measurement consisted of 40 on-peak baseline measurements of 4.2 s each, followed by 100 isotope ratio measurements of 8.4 s integration time each. Instrumental mass bias was corrected by internal normalization to ^{98}Mo/^{96}Mo = 1.453173 (denoted '8/6'), using the exponential law. The W, Pt, and Mo isotope data are reported in ε-notation as parts per 10^4 deviations relative to the isotopic ratios measured for pure, commercially available terrestrial bracketing solution standards (Alfa Aesar in case of Pt and Mo, NIST 3163 in case of W). The reported ε^iW, ε^iPt, and ε^iMo values for samples represent the mean of pooled solution replicates ($N = 1$–7) together with their associated external uncertainties (2s.d. or 95% conf. limits).

The accuracy and reproducibility of the Pt, W, and Mo isotope measurements were assessed through repeated analyses of a terrestrial metal standard (NIST SRM 129c) that was processed and analyzed alongside the meteorite metal samples. The Pt, Mo, and W isotopic compositions for NIST129c obtained are generally indistinguishable from previous measurements of this standard and the terrestrial bracketing standards (Tables 1–3, S1, S2), indicating that

the analyses are accurate to within the stated level of precision. For W, we also analyzed a sample of the IVB iron meteorite Skookum that was analyzed in a previous study (Kruijer et al., 2014b). The ε^iW values obtained for this sample are in excellent agreement with that measured in prior work (Table 2). Prior W isotope studies by MC-ICPMS observed small, but resolvable excesses in ε^{183}W (6/4), and corresponding excesses in ε^{182}W (6/3) for processed standards, most probably caused by a mass-independent W isotope fractionation induced during redissolution of W in Savillex beakers (e.g., Kruijer and Kleine, 2018; Willbold et al., 2011). Although the W isotope systematics of some NIST129c analyses are consistent with this effect, the overall magnitude is much smaller than in prior studies (Kruijer and Kleine, 2018; Kruijer et al., 2014b) and within the analytical uncertainty. Hence, in the present work any putative mass-independent effect on W isotopes is essentially negligible.

3. Results

3.1. Pt isotopes and CRE corrections

The pallasite samples are characterized by variable excesses in ε^{192}Pt (8/5) (up to ca. +23), ε^{194}Pt (8/5) (up to ca. +0.75), and ε^{196}Pt (8/5) (up to ca. +0.65) (Table 1). These Pt isotope variations are consistent with the predicted effects of secondary neutron capture reactions induced during CRE (Kruijer et al., 2013; Wittig et al., 2013). However, several other pallasite samples (Admire, Giroux, Newport, Marjalahti, Mount Vernon, Brenham, Eagle Station) exhibit Pt isotopic compositions indistinguishable from the terrestrial standards (Fig. 1, Table 1), indicating that any CRE effects are minor to absent for these samples. For ε^{192}Pt and ε^{194}Pt, the governing neutron capture reactions are ^{191}Ir$(n, \gamma)^{192}$Ir$(\beta^-)^{192}$Pt

Table 2

Tungsten isotopic compositions and Hf-W model ages of pallasites and iron meteorites.

Meteorite	Collection ID	ID	Hf[a] (ng/g)	W[a] (ng/g)	N[b]	Normalized to ^{186}W/^{183}W		Normalized to ^{186}W/^{184}W			Δt_{CAI}[e] (Ma)
						ε^{182}W$_{meas.}$[c]	ε^{184}W$_{meas.}$[c]	ε^{182}W$_{meas.}$[c]	ε^{183}W$_{meas.}$[c]	ε^{182}W$_{pre-exp.}$[d]	
Main-group (MG) pallasites											
Admire	USNM 703	DE07	0.03	108	2	-3.56 ± 0.09	-0.06 ± 0.07	-3.45 ± 0.09	0.09 ± 0.10	-3.45 ± 0.09	0.4 ± 1.0
Ahumada	ME 780 #30	DE06	0.03	104	1	-3.79 ± 0.09	-0.05 ± 0.07	-3.68 ± 0.10	0.08 ± 0.10		
Ahumada (Replicate)	ME 780 #30	DG12	0.16	118	1	-3.74 ± 0.09	-0.04 ± 0.07	-3.66 ± 0.11	0.06 ± 0.10		
Ahumada (Weighted mean, $N = 2$)	ME 780 #30	DE06				-3.76 ± 0.07	-0.05 ± 0.05	-3.67 ± 0.08	0.07 ± 0.07	-3.26 ± 0.13	2.0 ± 1.3
Brenham	ME1272 #3	DE01	0.0004	225	4	-3.59 ± 0.09	-0.07 ± 0.06	-3.47 ± 0.12	0.09 ± 0.09		
Brenham (Replicate)	ME1272 #3	DK01	ND	ND	5	-3.36 ± 0.12	0.01 ± 0.04	-3.39 ± 0.04	-0.02 ± 0.06		
Brenham (Weighted mean, $N = 2$)	ME1272 #3	DE01				-3.50 ± 0.07	-0.01 ± 0.04	-3.39 ± 0.04	0.01 ± 0.05	-3.39 ± 0.04	0.8 ± 0.7
Giroux	USNM 1574	DE08	0.07	120	1	-3.55 ± 0.09	-0.06 ± 0.07	-3.43 ± 0.09	0.09 ± 0.10	-3.43 ± 0.09	0.5 ± 1.0
Huckitta	USNM 6857	DG01	0.08	366	5	-3.80 ± 0.02	0.01 ± 0.04	-3.81 ± 0.06	-0.01 ± 0.06	-3.29 ± 0.12	1.7 ± 1.2
Imilac	ME 1267 #14	DE02	0.20	159	5	-3.75 ± 0.11	-0.01 ± 0.06	-3.73 ± 0.06	0.02 ± 0.10	-3.29 ± 0.12	1.7 ± 1.2
Imilac	USNM 2180	DG07	0.21	149	2	-3.86 ± 0.09	-0.05 ± 0.07	-3.76 ± 0.09	0.08 ± 0.10	-3.43 ± 0.16	0.5 ± 1.4
Krasnojarsk	LLNL	DB03	ND	ND	3	-3.33 ± 0.11	0.03 ± 0.06	-3.38 ± 0.12	-0.04 ± 0.09	-3.18 ± 0.16	2.8 ± 1.6
Marjalahti	BM.1920,318	DG04	0.04	254	5	-3.44 ± 0.05	-0.03 ± 0.04	-3.39 ± 0.05	0.04 ± 0.06	-3.25 ± 0.11	2.1 ± 1.1
Mount Vernon	USNM 300	DG09	1.83	171	1	-3.36 ± 0.09	0.05 ± 0.07	-3.46 ± 0.10	-0.07 ± 0.10	-3.37 ± 0.14	1.0 ± 1.3
Pavlodar	LLNL	DB04	ND	ND	6	-3.47 ± 0.06	0.02 ± 0.05	-3.51 ± 0.07	-0.03 ± 0.08	-3.29 ± 0.09	1.8 ± 1.0
Springwater	USNM 7816	DE05	0.012	102	1	-3.75 ± 0.09	-0.07 ± 0.07	-3.61 ± 0.11	0.10 ± 0.10	-3.22 ± 0.15	2.4 ± 1.5
MG pallasites with elevated ε^{182}W											
Acomita	ME 3382	DG05	0.42	157	1	-3.20 ± 0.09	0.00 ± 0.07	-3.20 ± 0.09	0.01 ± 0.10	-2.96 ± 0.14	5.2 ± 1.7
Newport	USNM 847	DG03	0.05	159	1	-3.05 ± 0.09	0.04 ± 0.07	-3.12 ± 0.10	-0.05 ± 0.10	-2.93 ± 0.16	5.6 ± 2.0
South Bend	ME 607 #14	DG02	0.07	191	4	-2.90 ± 0.07	-0.01 ± 0.08	-2.87 ± 0.11	0.02 ± 0.12	-2.59 ± 0.15	10.7 ± 2.6
Thiel Mountains	USNM 2180	DG06	0.20	128	1	-2.90 ± 0.09	0.03 ± 0.07	-2.97 ± 0.10	-0.05 ± 0.10	-2.72 ± 0.14	8.5 ± 2.1
Ungrouped pallasites											
Vermillion	USNM 6851	DE03	0.192	382	7	-4.24 ± 0.05	-0.01 ± 0.04	-4.22 ± 0.06	0.01 ± 0.05	-3.30 ± 0.12	1.6 ± 1.2
Eagle Station (PES) pallasites											
Eagle Station[f]	ME180#5	DK02	ND	ND	5	-3.17 ± 0.04	-0.08 ± 0.05	-3.01 ± 0.08	0.12 ± 0.08	-3.18 ± 0.14	2.8 ± 1.5
IIIAB iron meteorites											
Thunda	Münster	Z03	ND	ND	5	-2.97 ± 0.09	0.05 ± 0.05	-3.05 ± 0.03	-0.08 ± 0.07		
Thunda (Replicate)	Münster	AG02	ND	ND	5	-2.96 ± 0.06	0.06 ± 0.03	-3.06 ± 0.07	-0.09 ± 0.05		
Thunda (Weighted mean, $N = 2$)						-2.96 ± 0.05	0.06 ± 0.03	-3.05 ± 0.03	-0.09 ± 0.04	-2.86 ± 0.07	6.5 ± 2.4
IVB iron meteorites											
Skookum	USNM 5362	DB01	ND	ND	7	-3.49 ± 0.07	-0.11 ± 0.02	-3.27 ± 0.04	0.16 ± 0.03	ND	

[a] Hf and W concentrations were determined on solution aliquots by isotope dilution following the methods described in Kleine et al. (2004).

[b] N = Number of solution replicate analyses. One single analysis comprises 200 isotope ratio measurements of 4.2 s integration time each.

[c] Tungsten isotopic ratios are normalized to either ^{186}W/^{183}W = 1.9859 or ^{186}W/^{184}W = 0.92767 using the exponential law. The uncertainties reported for measured ε^{i}W values of samples (subscript "meas.") are based on the 2s.d. obtained from repeated (single) W isotope measurements of the terrestrial standard NIST129c (see Table S2) in the case $N < 4$ or in the case $N > 4$, the 95% conf. interval of the mean [i.e., according to (s.d. $\times t_{0.95,N-1})/\sqrt{N}$] calculated using solution replicate analyses of the individual sample. However, in the case that the standard error (2s.e.) based on internal run statistics of an individual sample exceeded the long-term reproducibility (2s.d.) of NIST129c, then the former 2s.e. errors are reported instead.

[d] Pre-exposure ε^{182}W (6/4) (subscript "pre-exp.") were calculated by correcting measured ε^{182}W (6/4) values for CRE effects using their re-normalized ε^{196}Pt (Table 1) and an average slope of -1.320 ± 0.055 (95% conf.) obtained from Pt-W isotope systematics of irradiated iron meteorites (Kruijer et al., 2017) using the following relation: ε^{182}W$_{pre-exposure} = \varepsilon^{182}W_{meas.} - [\varepsilon^{196}Pt_{meas.} + 0.06(\pm 0.01)] \times (-1.320 \pm 0.055)$ (Spitzer et al., 2021). Uncertainties on ε^{182}W (6/4)$_{pre-exp.}$ include propagated errors from the average slope, as well as ε^{182}W and ε^{196}Pt values.

[e] Hf-W model ages (Δt_{CAI}) were calculated relative to the Solar System initial ε^{182}W of -3.49 ± 0.07 for CAIs (Kruijer et al., 2014a), the present-day chondritic ε^{182}W of -1.9 ± 0.1 (Kleine et al., 2004), and using a ^{182}Hf decay constant of 0.078 Ma^{-1}.

[f] Reported pre-exposure ε^{182}W of Eagle Station represents measured ε^{182}W corrected for nucleosynthetic W isotope heterogeneity (see Section 3.2 and Kruijer et al., 2014a). ND = Not determined. Note that all W isotope measurements were performed at LLNL with the exception of IIIAB iron Thunda, which was analyzed in Münster.

and ^{193}Ir$(n, \gamma)^{194}$Ir$(\beta^-)^{194}$Pt and so the CRE effects depend on a sample's Ir/Pt. The samples of this study with previously reported Ir/Pt (e.g., Huckita, Pavlodar, Vermillion) plot on neutron capture model lines with distinct slopes that are consistent with their measured Ir/Pt (Fig. 1). Together, our results demonstrate that many pallasite metal samples exhibit neutron capture effects on Pt isotopes that are similar to those observed for iron meteorites.

The Pt isotopic signatures provide a suitable proxy for quantifying any CRE effects on W and Mo isotope compositions of meteorite metal samples (Kruijer et al., 2013, 2014b; Spitzer et al., 2020; Wittig et al., 2013; Worsham et al., 2017). As in previous studies, we use ε^{196}Pt (8/5) for the quantification of these effects, because this normalization reflects neutron capture effects on Pt isotopes only [i.e., through the reaction ^{195}Pt$(n, \gamma)^{196}$Pt] and hence is independent of the sample's Ir/Pt. Recently, Spitzer et al.

(2021) identified small nucleosynthetic isotope anomalies in some ungrouped iron meteorites, and showed that the most appropriate pre-exposure (i.e., unaffected by secondary neutron capture) ε^{196}Pt of meteorites is -0.06 ± 0.01. We follow this approach and also used this ε^{196}Pt as the pre-exposure composition of the pallasites of this study. With this assumption, neutron capture effects can be corrected using correlations of the isotope ratio of interest (i.e., ε^{182}W or ε^{i}Mo) with the neutron dosimeter (ε^{196}Pt), where the intercept at ε^{196}Pt $= -0.06 \pm 0.01$ provides the common pre-exposure ε^{182}W or ε^{i}Mo value of a specific meteorite group (Kruijer et al., 2013; Spitzer et al., 2020). Alternatively, the W or Mo isotopic compositions of samples can be corrected individually for CRE effects using their measured ε^{196}Pt alongside known ε^{182}W vs. ε^{196}Pt or ε^{i}Mo vs. ε^{196}Pt slopes obtained from CRE-induced correlations defined by other samples.

Table 3

Molybdenum isotopic compositions of pallasites.

Sample	Source	ID	N^a	ε^{92}Mo (±95% CI)	ε^{94}Mo (±95% CI)	ε^{95}Mo (±95% CI)	ε^{97}Mo (±95% CI)	ε^{100}Mo (±95% CI)	ε^{92}Mo[b] (±95% CI)	ε^{94}Mo[b] (±95% CI)	ε^{95}Mo[b] (±95% CI)	ε^{97}Mo[b] (±95% CI)	ε^{100}Mo[b] (±95% CI)
Main-group (MG) pallasites													
Acomita	ME 3382	DG05	8	1.10 ± 0.20	0.98 ± 0.18	0.50 ± 0.08	0.30 ± 0.03	0.25 ± 0.11	1.19 ± 0.21	1.04 ± 0.18	0.57 ± 0.08	0.32 ± 0.03	0.23 ± 0.11
Admire	USNM 703	DE07	5	1.29 ± 0.24	1.05 ± 0.11	0.49 ± 0.11	0.30 ± 0.04	0.25 ± 0.12	1.29 ± 0.24	1.05 ± 0.11	0.49 ± 0.11	0.30 ± 0.04	0.25 ± 0.12
Ahumada	ME 780 #30	DE06	5	1.16 ± 0.28	0.92 ± 0.16	0.37 ± 0.10	0.27 ± 0.03	0.35 ± 0.07	1.31 ± 0.28	1.01 ± 0.16	0.50 ± 0.10	0.30 ± 0.03	0.31 ± 0.07
Brenham	ME1272 #3	DE01	5	1.10 ± 0.28	0.97 ± 0.17	0.48 ± 0.09	0.30 ± 0.08	0.23 ± 0.11	1.12 ± 0.28	0.98 ± 0.17	0.50 ± 0.09	0.30 ± 0.08	0.23 ± 0.11
Giroux	USNM 1574	DE08	5	1.24 ± 0.20	1.06 ± 0.11	0.51 ± 0.09	0.26 ± 0.08	0.27 ± 0.11	1.24 ± 0.20	1.06 ± 0.11	0.51 ± 0.09	0.26 ± 0.08	0.27 ± 0.11
Huckitta	USNM 6857	DG01	6	0.92 ± 0.12	0.86 ± 0.09	0.33 ± 0.10	0.27 ± 0.07	0.29 ± 0.13	1.12 ± 0.13	0.98 ± 0.10	0.49 ± 0.11	0.31 ± 0.07	0.25 ± 0.13
Imilac	ME 1267 #14	DE02	5	1.12 ± 0.16	1.00 ± 0.08	0.42 ± 0.05	0.27 ± 0.04	0.29 ± 0.13	1.29 ± 0.17	1.10 ± 0.08	0.56 ± 0.06	0.30 ± 0.05	0.25 ± 0.13
Imilac	USNM 2180	DG07	8	0.99 ± 0.17	0.93 ± 0.14	0.34 ± 0.08	0.24 ± 0.06	0.27 ± 0.09	1.12 ± 0.17	1.01 ± 0.15	0.44 ± 0.09	0.26 ± 0.06	0.24 ± 0.09
Krasnojarsk	LLNL	DB03	5	1.12 ± 0.22	1.02 ± 0.15	0.46 ± 0.10	0.27 ± 0.04	0.24 ± 0.11	1.20 ± 0.22	1.07 ± 0.15	0.52 ± 0.11	0.28 ± 0.05	0.22 ± 0.11
Marjalahti	BM.1920,318	DG04	8	1.15 ± 0.17	1.04 ± 0.17	0.47 ± 0.06	0.29 ± 0.05	0.21 ± 0.11	1.20 ± 0.17	1.08 ± 0.17	0.51 ± 0.07	0.30 ± 0.05	0.20 ± 0.11
Mount Vernon	USNM 300	DG09	8	1.19 ± 0.09	1.05 ± 0.09	0.49 ± 0.04	0.28 ± 0.04	0.20 ± 0.08	1.19 ± 0.09	1.05 ± 0.09	0.49 ± 0.04	0.28 ± 0.04	0.20 ± 0.08
Newport	USNM 847	DG03	8	1.17 ± 0.12	1.01 ± 0.06	0.52 ± 0.08	0.31 ± 0.05	0.27 ± 0.08	1.25 ± 0.13	1.06 ± 0.07	0.58 ± 0.09	0.33 ± 0.05	0.25 ± 0.08
Pavlodar	LLNL	DB04	5	1.11 ± 0.20	1.09 ± 0.12	0.46 ± 0.03	0.27 ± 0.02	0.30 ± 0.12	1.19 ± 0.20	1.14 ± 0.13	0.53 ± 0.03	0.29 ± 0.02	0.28 ± 0.12
South Bend	ME 607 #14	DG02	8	1.16 ± 0.12	1.06 ± 0.09	0.45 ± 0.06	0.31 ± 0.04	0.32 ± 0.09	1.26 ± 0.13	1.13 ± 0.09	0.54 ± 0.07	0.33 ± 0.04	0.29 ± 0.09
Springwater	USNM 7816	DE05	5	1.10 ± 0.33	0.98 ± 0.21	0.43 ± 0.14	0.24 ± 0.04	0.28 ± 0.18	1.25 ± 0.34	1.07 ± 0.21	0.55 ± 0.14	0.27 ± 0.04	0.25 ± 0.19
Thiel Mountains	USNM 2180	DG06	8	1.15 ± 0.10	0.95 ± 0.06	0.49 ± 0.06	0.30 ± 0.06	0.21 ± 0.10	1.24 ± 0.11	1.01 ± 0.07	0.56 ± 0.07	0.31 ± 0.06	0.19 ± 0.10
Ungrouped pallasites													
Vermillion	USNM 6851	DE03	5	0.85 ± 0.20	0.74 ± 0.11	0.21 ± 0.11	0.18 ± 0.06	0.26 ± 0.18	1.20 ± 0.21	0.96 ± 0.12	0.48 ± 0.12	0.24 ± 0.07	0.18 ± 0.19
Eagle Station (PES) pallasites													
Eagle Station	ME180#5	DK02	8	1.79 ± 0.15	1.29 ± 0.09	1.09 ± 0.07	0.54 ± 0.05	0.59 ± 0.10	1.79 ± 0.15	1.29 ± 0.09	1.09 ± 0.07	0.54 ± 0.05	0.59 ± 0.10
Terrestrial standard													
BCR-2			5	-0.14 ± 0.20	-0.07 ± 0.14	-0.05 ± 0.07	0.00 ± 0.07	-0.01 ± 0.11					

Molybdenum isotopic ratios are normalized to ^{98}Mo/^{96}Mo = 1.453173 using the exponential law. Reported uncertainties are 95% conf. intervals (CI) of the mean [i.e., according to (s.d. $\times\ t_{0.95,N-1})/\sqrt{N}$] based on multiple solution replicate measurements.

[a] N = Number of solution replicate analyses. One single analysis comprises 100 isotope ratio measurements of 8.4 s integration time each.

[b] Molybdenum isotopic compositions corrected for CRE effects. CRE-corrected ε^iMo values were calculated using the weighted mean ε^iMo $vs.$ ε^{196}Pt slopes determined for NC iron meteorite groups (-0.46 ± 0.14 for ε^{92}Mo, -0.296 ± 0.059 for ε^{94}Mo, -0.37 ± 0.12 for ε^{95}Mo, -0.081 ± 0.084 for ε^{97}Mo, and 0.130 ± 0.058 for ε^{100}Mo) from Spitzer et al. (2020) and the re-normalized ε^{196}Pt for each pallasite following Spitzer et al. (2021).
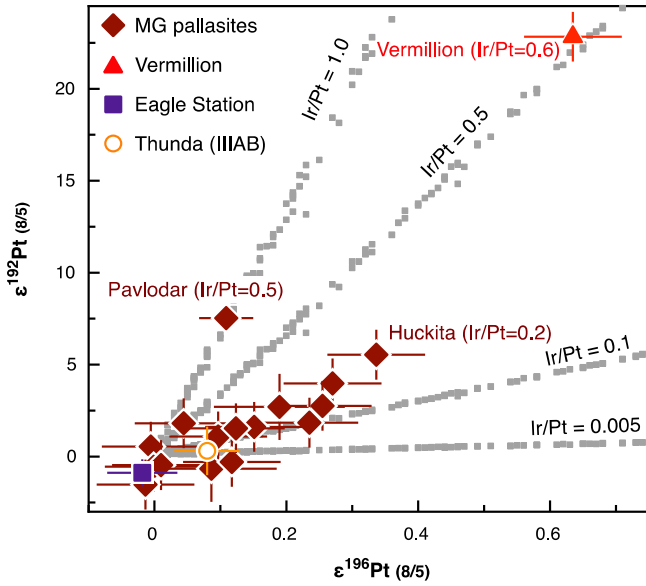
Fig. 1. Measured ε^{192}Pt (8/5) *vs.* ε^{196}Pt (8/5) for the pallasites and IIIAB iron Thunda analyzed in this study. Grey squares represent modeled predictions for secondary neutron capture (Kruijer et al., 2013). Error bars denote external uncertainties (95% conf. or 2s.d., see text). Ir/Pt for Huckita, Pavlodar and Vermillion are from Wasson and Choi (2003). (For interpretation of the colors in the figure(s), the reader is referred to the web version of this article.)

3.2. CRE-corrected W isotope results

All investigated main-group samples exhibit large and variable deficits in measured ε^{182}W ranging from ca. -3.8 to ca. -2.9 (Table 2). The ε^{182}W of Eagle Station (-3.01 ± 0.08, 95% conf.) falls within this range, whereas the ungrouped pallasite Vermillion (-4.22 ± 0.06, 95% conf.) exhibits the largest ε^{182}W deficit of the pallasites of this study. This range in ε^{182}W values among the pallasites is generally consistent with those reported in a prior study (Quitte et al., 2005), but more precise by a factor of 2-3, reflecting advances in measurement techniques. Overall, the observed range in ε^{182}W among the pallasites is similar to that observed for magmatic and non-magmatic iron meteorites (e.g., Hunt et al., 2018; Kruijer et al., 2017; Kruijer and Kleine, 2019; Kruijer et al., 2014b; Worsham et al., 2017). As for iron meteorites, most main-group pallasites exhibit correlated ε^{182}W (6/4) *vs.* ε^{196}Pt (8/5) variations (Fig. 2a), yielding a pre-exposure ε^{182}W of -3.31 ± 0.06 (95% conf., $N = 12$). The ungrouped pallasite Vermillion has the highest ε^{196}Pt and largest ε^{182}W deficit of the investigated pallasites, and plots on the extension of the ε^{182}W *vs.* ε^{196}Pt correlation line defined by the MG pallasites (Fig. 2a). Including this sample in the regression yields a combined pre-exposure ε^{182}W for the main-group pallasites and Vermillion of -3.31 ± 0.05 (95% conf., $N = 13$). The ε^{182}W *vs.* ε^{196}Pt slope for the pallasites obtained by linear regression (-1.30 ± 0.19, 95% conf.) is in excellent agreement with the mean slope obtained for magmatic iron meteorites (-1.320 ± 0.055, 95% conf.) (Kruijer et al., 2017). Hence, the relative magnitude of secondary neutron capture effects on Pt and W isotopes is very similar in iron meteorites and pallasites and thus is not significantly affected by different metal-to-olivine ratios.

Some MG pallasites (Acomita, Newport, Sound Bend, Thiel Mountains) plot above the ε^{182}W *vs.* ε^{196}Pt correlation line defined by the majority of MG pallasites, indicating that the ε^{182}W variations are not solely caused by CRE effects. For these samples, CRE-effects must be corrected individually, using the measured ε^{196}Pt for each sample together with the mean slope obtained for ε^{182}W *vs.* ε^{196}Pt correlation lines of magmatic iron meteorites and
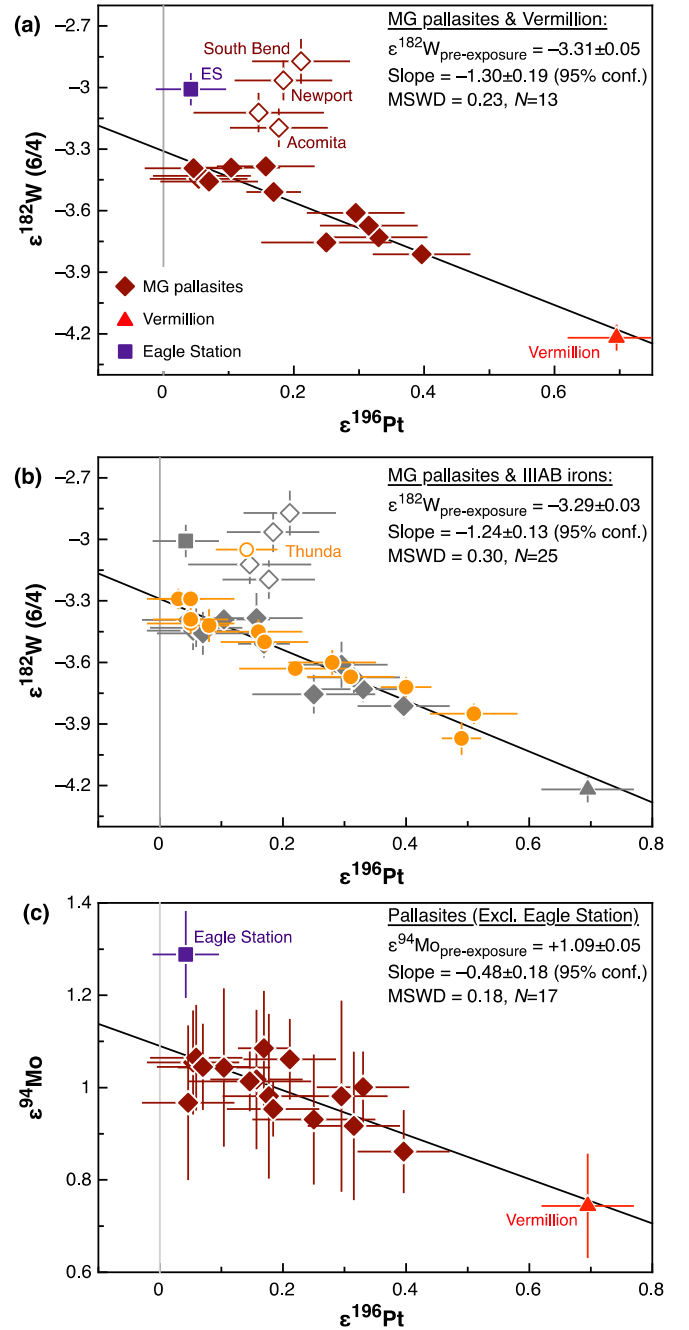
Fig. 2. (a) ε^{182}W *vs.* ε^{196}Pt for pallasites analyzed in this study, and (b) pallasite results (grey symbols) shown in comparison to data for IIIAB iron meteorites from this and prior work (Kruijer et al., 2014b). (c) ε^{94}Mo *vs.* ε^{196}Pt for pallasites in this study. Note that the ε^{196}Pt data were re-normalized to a pre-exposure ε^{196}Pt of -0.06 ± 0.01 (95% conf.) following Spitzer et al. (2021). Error bars denote external uncertainties (95% conf. or 2s.d., see text). Solid lines show best-fit linear regression lines through the data calculated using IsoplotR. MG pallasites and IIIAB irons with elevated ε^{182}W (open symbols) and Eagle Station (ES) were not included in ε^{182}W *vs.* ε^{196}Pt regressions. Ungrouped pallasite Vermillion plots on the extension of all CRE–induced correlation lines but was only included in the regression shown in (a) and (c). See Fig. 1 for legend of pallasite samples.

using the relation ε^{182}W$_{pre-exposure} = \varepsilon^{182}W_{meas.} - [\varepsilon^{196}Pt_{meas.} + 0.06(\pm0.01)] \times (-1.320 \pm 0.055)$ (Spitzer et al., 2021). The resulting ε^{182}W$_{pre-exposure}$ for these samples are considerably more elevated than for other MG pallasites (Table 2, Fig. 4). Similarly, the newly analyzed IIIAB iron meteorite Thunda plots above the ε^{182}W *vs.* ε^{196}Pt correlation line defined by other IIIAB irons and exhibits a relatively elevated pre-exposure ε^{182}W of -2.86 ± 0.07 (95%

conf.), significantly higher than the pre-exposure ε^{182}W of -3.27 $\pm$ 0.03 (95% conf.) of IIIAB iron meteorites (Kruijer et al., 2014b) when corrected using their revised pre-exposure ε^{196}Pt (Spitzer et al., 2021).

Unlike for ^{182}W, CRE does not affect internally normalized ^{183}W/^{184}W ratios. However, ε^{183}W may vary as a result of nucleosynthetic isotope variability and prior studies have shown that CC meteorites are characterized by small ε^{183}W excesses (e.g., Qin et al., 2008), while NC meteorites show no resolved ^{183}W anomalies relative to the terrestrial standard (Hilton and Walker, 2020; Kruijer and Kleine, 2019; Kruijer et al., 2014b). Consistent with this, the results of this study show that all MG pallasites and Vermillion exhibit a narrow range in ε^{183}W that is indistinguishable from the terrestrial standard (Table 2), yielding a mean ε^{183}W of 0.02 $\pm$ 0.03 (95% conf., $N = 17$). By contrast, Eagle Station exhibits a resolved excess in ε^{183}W of $+0.12 \pm 0.08$ (95% conf. $N = 5$), consistent with that observed for magmatic iron meteorites from the CC reservoir (Hilton et al., 2019; Kruijer et al., 2017). The effects of nucleosynthetic heterogeneity on ε^{182}W can be quantified using the ε^{183}W of a sample and the empirically defined linear relations between nucleosynthetic ε^{182}W and ε^{183}W variations (Kruijer et al., 2014a). Correcting the measured ε^{182}W of Eagle Station using this approach, yields a corrected ε^{182}W value of -3.18 ± 0.14 (95% conf.), which is very similar to the pre-exposure ε^{182}W compositions of magmatic iron meteorite groups originating from the CC reservoir (e.g., IIC, IID, IIF, IIIF, IVB) (Hilton et al., 2019; Kruijer et al., 2017; Tornabene et al., 2020) after accounting for nucleosynthetic Pt isotope heterogeneity (Spitzer et al., 2021).

3.3. CRE-corrected Mo isotope results

All pallasites analyzed here exhibit resolved ε^{i}Mo anomalies relative to the terrestrial standard (Table 3, Fig. 2c, 3a). The results for Brenham and Eagle Station agree with previous data (Burkhardt et al., 2011), but are more precise. Moreover, like iron meteorites, the MG pallasites exhibit small ε^{i}Mo variations that correlate with ε^{196}Pt (Fig. 2c), indicating the presence of superimposed cosmic ray–induced effects (Spitzer et al., 2020; Worsham et al., 2017). These CRE effects were corrected using the ε^{i}Mo vs. ε^{196}Pt slope previously derived from results for magmatic iron meteorite groups (Spitzer et al., 2020). After correction for CRE effects, all MG pallasites and Vermillion have indistinguishable ε^{i}Mo compositions (Fig. 3, Table 3), indicating there are no resolvable nucleosynthetic Mo isotope variations among the MG pallasites and the ungrouped pallasite Vermillion. By contrast, the Mo isotope composition of Eagle Station is markedly distinct from the other pallasites. For instance, Eagle Station has a ε^{95}Mo value of $+1.09 \pm 0.07$ (95% conf.), considerably more elevated than the mean ε^{95}Mo of $+0.54 \pm 0.03$ (95% conf.) obtained for the MG pallasites and Vermillion. Finally, in a plot of ε^{95}Mo vs. ε^{94}Mo (Fig. 3), where bulk meteorites plot on two distinct s-process mixing lines termed the NC and CC lines (Budde et al., 2016), all MG pallasites and Vermillion plot on the NC line, whereas Eagle Station plots on the CC line. These observations corroborate prior results (Burkhardt et al., 2011; Lugmair and Shukolyukov, 1998; Warren, 2011) indicating that MG pallasites derive from the inner disk (NC reservoir), whereas Eagle Station originates from the outer disk (CC reservoir).

4. Discussion

4.1. Genetic and chronological links between main-group pallasites and IIIAB iron meteorites

#### 4.1.1. Genetic link inferred from Mo isotopes

A key result of this study is that after correction for CRE effects, the Mo isotope composition of all MG pallasites and Vermillion is
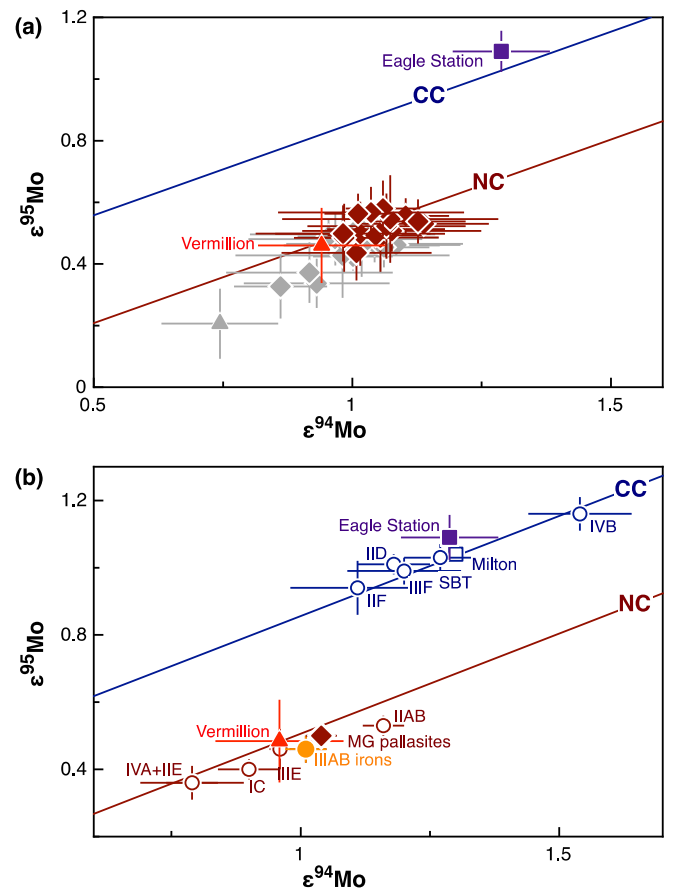
Fig. 3. (a) ε^{95}Mo vs. ε^{94}Mo for the pallasites analyzed in this study corrected (colored symbols) and uncorrected (grey symbols) for CRE effects. (b) Mo isotopic data of pallasites in comparison to mean values previously obtained for other meteorite groups. Slopes of NC and CC lines are based on Mo isotopic data for acid leachates and bulk meteorites from the NC and CC reservoirs (Budde et al., 2019; Spitzer et al., 2020). Molybdenum isotopic data of IIIAB iron meteorites and other meteorite groups are from the compilation reported in Spitzer et al. (2020) and data for the Milton pallasite and South Byron Trio (SBT) are from Hilton et al. (2019). Error bars denote external uncertainties (95% conf. or 2s.d., see text). See Fig. 1 for legend of pallasites.

indistinguishable from that of IIIAB irons (Fig. 3b). The Mo isotope similarity, alongside previously observed chemical similarity (Wasson and Choi, 2003), demonstrates that MG pallasites and IIIAB irons are genetically linked. This is consistent with the O isotope similarities previously observed between pallasite olivine and phosphates and chromites from IIIAB irons (Clayton and Mayeda, 1996; Greenwood et al., 2015). Nevertheless, the Mo isotope results establish the link between pallasites and IIIAB irons more directly, given that for both classes of meteorites metal samples were analyzed. By contrast, ungrouped pallasites, including Vermillion, have trace element compositions that are markedly different from MG pallasites, and on this basis, are argued to derive from a distinct parent body (Wasson and Choi, 2003). Although the Mo isotope composition of Vermillion overlaps with those of MG pallasites, it also is similar to several other iron meteorites such as the IC and IIIE irons (Fig. 3b). Thus, despite the similarity in Mo isotope compositions, our results do not rule out derivation of MG and ungrouped pallasites from distinct parent bodies.

The MG pallasites and Vermillion plot on the NC line, indicating that the metal in these samples derives from a relatively homogeneous reservoir with little to no contribution from CC bodies. Thus, in an impact formation scenario, the pallasite metal either derives entirely from one of the colliding bodies, or metal from two NC
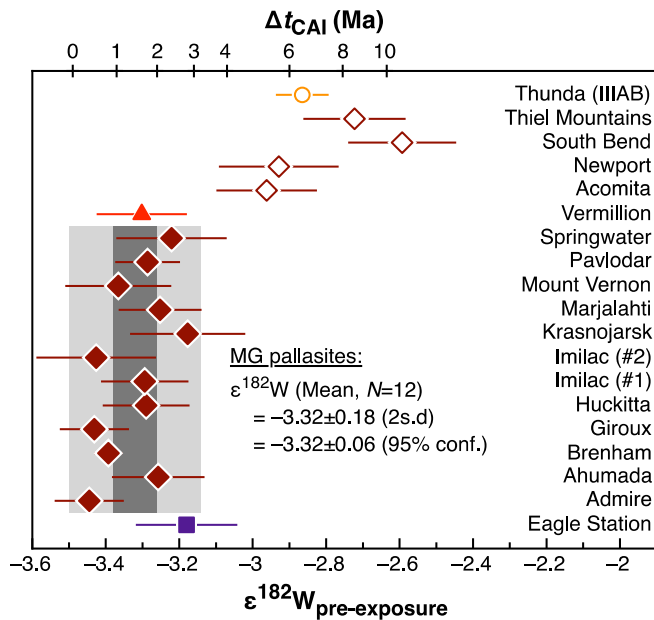
Fig. 4. Pre-exposure ε^{182}W of pallasites (and IIIAB iron Thunda) analyzed in this study and corresponding two-stage Hf-W model ages (Δt_{CAI}, in Ma) calculated relative to the time of CAI formation. Error bars denote propagated uncertainties on pre-exposure ε^{182}W values (2σ, see text). Pre-exposure ε^{182}W of Eagle Station was corrected for nucleosynthetic isotope heterogeneity. The mean ε^{182}W composition of the main-group (MG) pallasites and their external uncertainties are shown as light shaded (2 s.d.) and dark shaded areas (95% confidence intervals, $N = 12$). See Fig. 1 for legend.

bodies had been mixed and homogenized before it was incorporated into the MG pallasite parent body.

4.1.2. Chronological link inferred from Hf-W chronometry

A further key result of this study is that the pre-exposure ε^{182}W of MG pallasites (-3.31 ± 0.06) is essentially identical to that of IIIAB iron meteorites [-3.27 ± 0.03; (Kruijer et al., 2014b; Spitzer et al., 2021)]. This is perhaps best illustrated by the observation that IIIAB irons and MG pallasites define a single ε^{182}W vs. ε^{196}Pt correlation line (MSWD = 0.30) with a common intercept value of ε^{182}W = -3.29 ± 0.03 (95% conf., $N = 25$) (Fig. 2b). A Hf-W model age of metal-silicate separation can be calculated by assuming a single event of Hf-W fractionation from a reservoir with a chondritic Hf/W as follows:

$$\Delta t = -\frac{1}{\lambda} \ln \left[\frac{(\varepsilon^{182}W)_{Sample} - (\varepsilon^{182}W)_{Chondrites}}{(\varepsilon^{182}W)_{SSI} - (\varepsilon^{182}W)_{Chondrites}} \right] \qquad (2)$$

where $\varepsilon^{182}W_{SSI}$ represents the Solar System initial of -3.49 ± 0.07 (95% conf.) (Kruijer et al., 2014a), $\varepsilon^{182}W_{chondrites}$ is the present-day value of carbonaceous chondrites of -1.9 ± 0.1 (2σ) (Kleine et al., 2004) and λ is the decay constant of ^{182}Hf of 0.078 ± 0.002 Myr^{-1} (2σ). The common pre-exposure ε^{182}W of -3.29 ± 0.03 (95% conf.) for the MG pallasites and IIIAB irons yields a Hf-W model age of 1.7 ± 0.6 Ma (2σ) after CAI formation. Hellmann et al. (2019) showed that the precursors to ordinary chondrites were characterized by a much lower Hf/W than carbonaceous chondrites; if this value (^{180}Hf/^{184}W ≈ 0.7; corresponding to $\varepsilon^{182}W_{Chondrites} = -2.67$ in Eq. (2)) is assumed in the model age calculation, the Hf-W age for the MG pallasites and IIIAB irons changes to 3.6 ± 1.5 Ma.
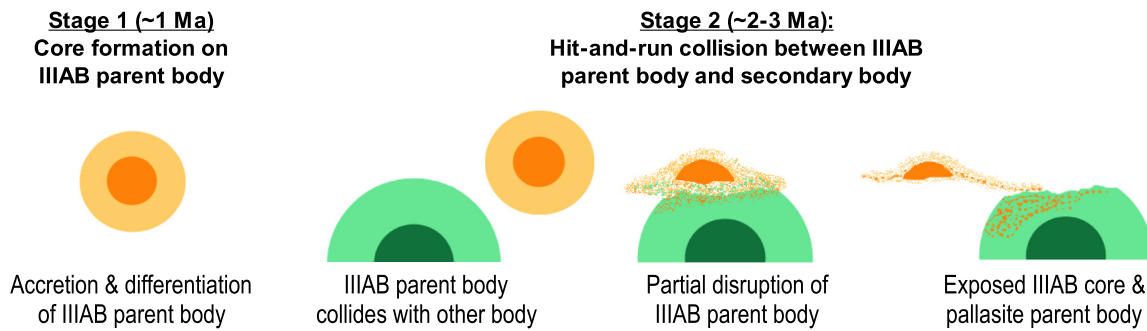
Four MG pallasites and the IIIAB iron Thunda have more radiogenic ^{182}W compositions than the majority of the pallasites and IIIAB irons, with pre-exposure ε^{182}W ranging from ca. -3.0 to -2.6 (Table 2, Fig. 4). These more radiogenic ε^{182}W values indicate

later metal-silicate separation in these samples or, alternatively, partial re-equilibration between silicates and metal after the initial metal segregation. The Hf-W model ages for these samples are $\sim$5-11 Ma after CAI formation, but these ages are only meaningful if metal and silicates completely equilibrated in their original chondritic proportions, or if the melting and metal segregation occurred from a chondritic, previously undifferentiated precursor (Kruijer and Kleine, 2019). As will be discussed in more detail below, this is unlikely to be the case in current formation models for pallasites, especially for scenarios that involve impact–induced mixing of metal and silicates.

Collectively, their virtually identical Hf-W systematics and Mo isotopic compositions demonstrate that MG pallasite metal and IIIAB irons derive from metallic melts with an identical heritage and history of metal-silicate separation. When the Hf-W systematics and Mo isotopes are considered individually, the similarity in Hf-W ages or isotopic makeup does not necessarily imply a link between any two samples. For instance, the non-magmatic iron meteorite groups IAB and IIE have very similar Hf-W systematics (Hilton and Walker, 2020; Hunt et al., 2018; Kruijer and Kleine, 2019; Worsham et al., 2017), indicating a virtually identical history of metal-silicate fractionation, yet have distinct mineralogy (Ruzicka, 2014), chemical compositions (Scott and Wasson, 1975), as well as Mo isotope compositions (Bermingham et al., 2018; Poole et al., 2017; Worsham et al., 2017), indicating that they derive from separate parent bodies. Conversely, IC irons, acapulcoites-lodranites, and ureilites have very similar Mo isotope compositions (Budde et al., 2019; Hopp et al., 2020; Spitzer et al., 2020), but different Hf-W ages (Kruijer et al., 2017; Touboul et al., 2009), indicating that they derive from similar nebular source materials but from different parent bodies that underwent distinct histories of heating, melting, and differentiation. However, the MG pallasites and IIIAB irons are uniquely linked because they are the only two meteorite groups that exhibit both identical Mo isotope compositions and Hf-W systematics. Although it cannot be excluded that two separate bodies formed from a similar mixture of nebular materials and underwent similar histories of melting and metal-silicate separation, such a coincidence appears rather unlikely. This is especially true given that IIIAB irons and pallasite metal are also chemically linked, suggesting that pallasites represent an evolved metallic melt consistent with evolved melts from the IIIAB core (Wasson and Choi, 2003). Together, these genetic, chronological, and chemical links suggest strongly that MG pallasite metal derives from the core of the IIIAB parent body.

4.2. Link between Eagle Station pallasites and CC iron meteorites

As for the MG pallasites and IIIAB irons, the Mo isotopic composition and ε^{182}W of Eagle Station are indistinguishable from those of many CC irons (e.g., IID, IIIF, South Byron Trio) (Fig. 3b). Thus, similar to the MG pallasites and IIIAB irons, these data suggest that the Eagle Station pallasite contains metal derived from the core of an iron meteorite parent body, but in this case from a body that originated in the CC reservoir. Pallasites from the CC reservoir also exhibit some general chemical similarities to CC iron meteorites, including higher FeO/(FeO + MgO) as well as higher concentrations of Ni and refractory siderophile elements than NC iron meteorites and MG pallasites (Rubin, 2018; Scott, 1977). However, unlike for MG pallasites and IIIAB irons, no clear chemical link exists between pallasites from the CC reservoir and a specific CC iron meteorite group. For instance, the Milton pallasite and the South Byron Trio iron meteorites, both CC meteorite groups, exhibit identical Mo, Ru and O isotopic compositions, but their highly siderophile element signatures cannot easily be related by fractional crystallization modeling (Hilton et al., 2019). Nevertheless, the genetic and chronological link between MG pallasites and IIIAB

Stage 1 (~1 Ma)
Core formation on
IIIAB parent body

Stage 2 (~2-3 Ma):
Hit-and-run collision between IIIAB
parent body and secondary body

Accretion & differentiation
of IIIAB parent body

IIIAB parent body
collides with other body

Partial disruption of
IIIAB parent body

Exposed IIIAB core &
pallasite parent body

Fig. 5. Two-stage formation model for MG pallasites. The formation of pallasites involved core formation on the IIIAB parent body at ∼1.7 Ma after CAIs, followed by a hit-and-run collision with another body at around 2-3 Ma. This collision caused partial disruption and (re)-melting of the IIIAB core, causing impact–induced mixing of metal and silicates, while another portion of the IIIAB core may have stayed intact. Molten IIIAB core material was subsequently injected into the mantle of the colliding body, resulting in the formation of MG pallasites.

irons on the one side, and between Eagle Station and CC irons on the other, suggests that pallasite formation in the inner (NC) and outer (CC) disk occurred by similar processes, and involved metal derived from planetesimal cores.

4.3. Origin of pallasites

In addition to the isotopic and chronological link observed in this study, MG pallasites and IIIAB irons are also chemically related. In element *vs.* Au diagrams, MG pallasites generally plot on the extension of fractional crystallization trends defined by IIIAB irons, but with substantial scatter. This has been interpreted to indicate that MG pallasite metal samples represent mixtures of late-stage liquids and early solids of the IIIAB core (Wasson and Choi, 2003). At face value, these close genetic, chronological, and chemical links appear consistent with formation of MG pallasites near the core-mantle boundary of the IIIAB parent body (Wasson and Choi, 2003). However, the different cooling histories of MG pallasites and IIIAB irons indicate that these meteorites derive from distinct parent bodies. More specifically, metallographic cooling rates of pallasites are much lower than those of IIIAB iron meteorites (Yang and Goldstein, 2006; Yang et al., 2010), and paleomagnetic evidence shows that pallasites cooled at lower temperature and shallower depth than expected for a core-mantle boundary (Bryson et al., 2015; Nichols et al., 2016; Tarduno et al., 2012). These seemingly contradictory observations can be reconciled if MG pallasites formed during the collisional disruption of the IIIAB parent body and associated impact–induced mixing of core and mantle material. This model is similar to previously proposed impact models for the origin of pallasites (Tarduno et al., 2012; Yang et al., 2010). Below we will discuss these and other models in more detail.

Derivation of MG pallasite metal from the IIIAB core implies that the chronology of IIIAB core cooling and crystallization provides important additional constraints for understanding MG pallasite formation. According to Pd-Ag isotope systematics, the IIIAB core crystallized at 2.6 ± 1.3 Ma after Solar System formation (Matthes et al., 2020). This rapid cooling and crystallization is most readily explained by a collisional disruption of the IIIAB parent body, which would have removed most of its silicate mantle and led to partial excavation of the IIIAB core. It is then conceivable that MG pallasites also formed during this event, through mixing of released IIIAB metal and mantle material from the IIIAB parent body or the colliding body. This is consistent with some existing models of pallasite formation involving impact–induced mixing of metal and silicates (Tarduno et al., 2012; Walte et al., 2020; Yang et al., 2010), but is more difficult to reconcile with formation of pallasites by ferrovolcanism (i.e., by intrusion of late-stage core liquids into the overlying silicate mantle of a differentiated body) on an intact body (Johnson et al., 2020). This is because without prior

stripping of the silicate mantle, cooling and crystallization of the IIIAB core would have lasted much longer than given by Pd-Ag chronometry (Matthes et al., 2020).

Walte et al. (2020) proposed a hybrid model in which MG pallasites contain two distinct metal populations, namely a small amount of indigenous metal from the pallasite parent body, which was left behind in the mantle during core formation, and a larger fraction of impactor-derived metal that was injected into the mantle upon impact. If pallasites indeed contain metal from different bodies, then Mo isotopic variations among the metal samples might be expected. However, the results from the present study do not reveal such variations, and hence do not provide direct evidence for the existence of more than one metal population. It may be possible that the two putative metal populations were isotopically homogenized on the pallasite parent body itself. In this case the similar Hf-W systematics of MG pallasites and IIIAB irons would be coincidental, however. This is because the re-equilibration of two metals in the mantle of the pallasite parent body should have also resulted in at least some ^{182}W re-equilibration between metal and surrounding silicates, leading to more elevated ε^{182}W values of MG pallasites relative to IIIAB irons. Although there are some MG pallasites with more elevated ε^{182}W, these samples do not exhibit distinct Mo isotopic compositions and the majority of MG pallasites have the same ε^{182}W as IIIAB irons (Fig. 4). It is also possible that the two colliding bodies had indistinguishable Mo isotope signatures, in which case the two putative metal populations cannot be distinguished based solely on Mo isotopes.

Based on the above considerations and building on some prior models for pallasite formation (Yang et al., 2010; Tarduno et al., 2012), we propose that pallasite metal mixed with mantle-derived silicates as a result of the collision that also led to the excavation of IIIAB core (Fig. 5). In this scenario, MG pallasite metal initially formed during segregation of the IIIAB core and was subsequently injected into the mantle of another body that collided with the IIIAB parent body and led to exposure of the IIIAB core. This model not only satisfies the geochemical and isotopic similarities of IIIAB iron meteorites and MG pallasites, but also their distinct cooling rates (Yang and Goldstein, 2006; Yang et al., 2010). Whereas IIIAB iron meteorites would have cooled relatively rapidly due to the partial excavation of their core (Matthes et al., 2020), pallasite metals would have cooled more slowly because they were rapidly embedded in silicates which may immediately have acted as an efficient insulator.

The collisional disruption of the IIIAB parent body would have mixed metals with unradiogenic ε^{182}W representative of the IIIAB core and silicates with more radiogenic ε^{182}W from the overlying mantle and/or that of the colliding body. Impact–induced mixing and isotopic equilibration, therefore, may explain the more radio-
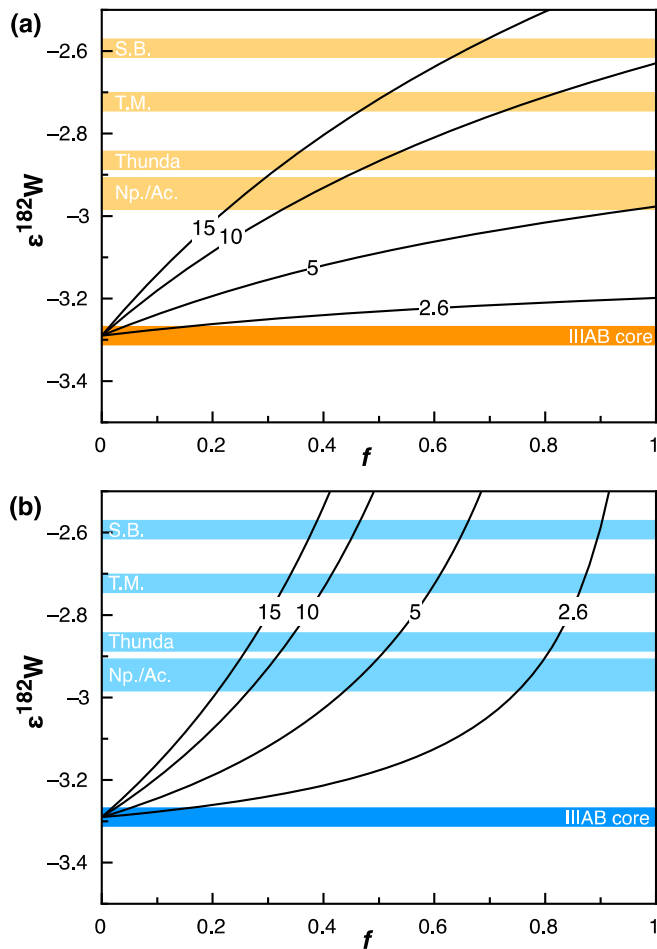
Fig. 6. Modeled effects of impact–induced mixing of core derived metal and mantle derived silicates, shown as ε^{182}W *vs.* the fraction of silicates (f) that the W in the metal equilibrated with. Shown are the effects for two scenarios: (a) Equilibration between IIIAB metal and silicates in chondritic proportions, *i.e.*, assuming that the core was mixed with the silicate mantle that it had previously separated from, and (b) Equilibration between IIIAB metal and a hypothetical silicate reservoir with elevated Hf/W similar to some eucrites (see text). Different curves show effects of mixing of W isotopes between metal and silicates at three different times (at 2.6, 5, 10, and 15 Ma after CAI formation). Solid bars show the pre-exposure ε^{182}W obtained for the IIIAB core, as well as for pallasites and IIIAB irons with elevated ε^{182}W, i.e., South Bend (S.B.), Thiel Mountains (T.M.), Acomita (Ac.), Newport (Np.), and Thunda. The model curves were calculated assuming that the IIIAB parent body had a carbonaceous chondrite like ^{180}Hf/^{184}W (Kleine et al., 2004) and a W concentration of 1000 ppb in the metal, *i.e.*, similar to that observed in IIIAB metal. Using a H chondrite-like ^{180}Hf/^{184}W (Hellmann et al., 2019) instead yields slightly shallower model curves, but overall identical conclusions. For the calculations we further used an initial ^{182}Hf/^{180}Hf of $(1.018 \pm 0.043) \times 10^{-4}$ and ε^{182}W $= -3.49 \pm 0.07$ (95% conf.) at the start of Solar System history as inferred based on CAIs (Kruijer et al., 2014a), and a decay constant for ^{182}Hf of $\lambda = 0.078$ Ma^{-1}.

genic pre-exposure ε^{182}W signatures of four main-group pallasites as well as of the IIIAB iron Thunda (Fig. 2b and 4). To more quantitatively assess this, we used the model presented in Kruijer and Kleine (2019) to calculate the ε^{182}W composition of metal resulting from mixing and isotopic equilibration at different times and with variable amounts of silicates (Fig. 6). In the simplest scenario the IIIAB metal would simply have partly mixed with silicates from the overlying mantle that it had previously separated from (Fig. 6a). In this case the radiogenic ε^{182}W signatures of the abovementioned meteorites can in principle be reproduced provided that (i) the impact causing the mixing of core-derived metal and mantle-derived silicates occurred relatively late (>15 Ma) and (ii) a significant fraction of the W in these meteorites (>60%) derives from mantle-derived silicates. However, as noted

above, impact–induced excavation of the IIIAB core likely occurred much earlier at 2.6 ± 1.3 Ma after CAIs (Matthes et al., 2020) and hence is inconsistent with such a late time of impact-induced mixing of metal and silicates. An alternative possibility is that the IIIAB core mixed with a hypothetical silicate reservoir so that metal and silicates were mixed in non-chondritic proportions. Although the Hf-W systematics of such a reservoir are not *a priori* known, it is useful to consider the effects of mixing between the IIIAB core and a hypothetical, high-Hf/W silicate source, for instance, like that of some basaltic eucrites, which also formed very early and have the most radiogenic ^{182}W signatures known among bulk meteorites (Touboul et al., 2015) (Fig. 6b). The calculations reveal that impact–induced mixing and isotopic equilibration at 2.6 Ma readily reproduces the radiogenic ε^{182}W of the four MG pallasites and Thunda, provided that W in the metal isotopically equilibrated with a very large fraction (>85%) of mantle-derived silicates. Although it cannot be fully ruled out that these silicates derive from a high Hf/W reservoir on the IIIAB parent body itself, it seems more likely that the required large silicate mass fraction reflects the contribution of mantle material from the colliding body to this mixing process.

The latter scenario would be consistent with the expected outcome of hit-and-run collisions between two different-sized objects (Asphaug et al., 2006). In such collisions, the mantle of the smaller objects is removed, resulting in a chain of metal-enriched bodies with varying amounts of silicates. The exposed IIIAB core would represent one (or several) of these bodies, while the MG pallasite parent body or bodies may have formed either by re-accretion of metallic melt and silicates or, alternatively, by injection of IIIAB core-derived liquid metal into the silicate mantle of the larger of the two colliding bodies (Tarduno et al., 2012) (Fig. 5). The latter would appear consistent with paleomagnetic evidence indicating that MG pallasite olivine originated in the shallow mantle of a relatively large ($R \sim 200$ km) differentiated parent body with core dynamo activity lasting several tens of Ma (Bryson et al., 2015; Tarduno et al., 2012), which requires that (part of) the core of this body remained molten for an extended period of time. This in turn suggests that, contrary to MG pallasite metal, the MG pallasite silicates did not originate on the IIIAB parent body but instead from the colliding body. This model may be tested by determining nucleosynthetic isotope signatures of an element that is measurable in both pallasite metal and silicates, to assess whether or not their heritage is different from that of the metal.

5. Conclusions

The MG pallasites of this study have ε^{182}W and Mo isotopic compositions that are indistinguishable from IIIAB iron meteorites, demonstrating that MG pallasite metal originated in the IIIAB core. This finding, combined with independent evidence for early and rapid excavation of the IIIAB core, implies that MG pallasites formed by impact–induced mixing of core-derived metal and mantle-derived silicates rather than by internal processes on the IIIAB parent body. Collectively, formation of MG pallasites thus very likely occurred in two stages, involving (i) early formation of pallasite metal in the IIIAB parent body core at 1.7 ± 0.6 Ma, followed by (ii) impact–induced mixing and partial re-equilibration of metal and silicates around 2-3 Ma. Although the silicates may in principle also derive from the IIIAB parent body mantle itself, the evidence for an early excavation of the IIIAB core renders it more likely that MG pallasite silicates originated from the colliding body. This formation model is chronologically consistent and can explain several observations, not only the chemical and isotopic similarities of MG pallasites and IIIAB irons, but also their diverse cooling rates and paleomagnetic evidence.

CRediT authorship contribution statement

Thomas S. Kruijer: Conceptualization, Funding acquisition, Investigation, Project administration, Validation, Visualization, Writing – original draft. **Christoph Burkhardt:** Investigation, Validation, Writing – review & editing. **Lars E. Borg:** Funding acquisition, Validation, Writing – review & editing. **Thorsten Kleine:** Conceptualization, Resources, Validation, Writing – review & editing.

Declaration of competing interest

The authors declare that they have no known competing financial interests or personal relationships that could have appeared to influence the work reported in this paper.

Acknowledgements

Appendix A. Supplementary material

Supplementary material related to this article can be found online at https://doi.org/10.1016/j.epsl.2022.117440.

References

Abrahams, J.N.H., Nimmo, F., 2019. Ferrovolcanism: iron volcanism on metallic asteroids. Geophys. Res. Lett. 46, 5055–5064.

Asphaug, E., Agnor, C.B., Williams, Q., 2006. Hit-and-run planetary collisions. Nature 439, 155–160.

Benedix, G.K., Haack, H., McCoy, T.J., 2014. Iron and stony-iron meteorites. In: Davis, A.M. (Ed.), Treatise on Geochemistry, vol. 1, second edition. Elsevier, Oxford, pp. 267–285.

Bermingham, K.R., Worsham, E.A., Walker, R.J., 2018. New insights into Mo and Ru isotope variation in the nebula and terrestrial planet accretionary genetics. Earth Planet. Sci. Lett. 487, 221–229.

Boesenberg, J.S., Delaney, J.S., Hewins, R.H., 2012. A petrological and chemical re-examination of Main Group pallasite formation. Geochim. Cosmochim. Acta 89, 134–158.

Bryson, J.F.J., Nichols, C.I.O., Herrero-Albillos, J., Kronast, F., Kasama, T., Alimadadi, H., van der Laan, G., Nimmo, F., Harrison, R.J., 2015. Long-lived magnetism from solidification-driven convection on the pallasite parent body. Nature 517, 472–475.

Budde, G., Burkhardt, C., Brennecka, G.A., Fischer-Gödde, M., Kruijer, T.S., Kleine, T., 2016. Molybdenum isotopic evidence for the origin of chondrules and a distinct genetic heritage of carbonaceous and non-carbonaceous meteorites. Earth Planet. Sci. Lett. 454, 293–303.

Budde, G., Burkhardt, C., Kleine, T., 2019. Molybdenum isotopic evidence for the late accretion of outer solar system material to Earth. Nat. Astron. 3, 736–741.

Burkhardt, C., Kleine, T., Oberli, F., Pack, A., Bourdon, B., Wieler, R., 2011. Molybdenum isotope anomalies in meteorites: constraints on solar nebula evolution and origin of the Earth. Earth Planet. Sci. Lett. 312, 390–400.

Clayton, R.N., Mayeda, T.K., 1996. Oxygen isotope studies of achondrites. Geochim. Cosmochim. Acta 60, 1999–2017.

Dauphas, N., Marty, B., Reisberg, L., 2002. Molybdenum evidence for inherited planetary scale isotope heterogeneity of the Protosolar Nebula. Astrophys. J. 565, 640–644.

Dottin, J.W., Farquhar, J., Labidi, J., 2018. Multiple sulfur isotopic composition of main group pallasites support genetic links to IIIAB iron meteorites. Geochim. Cosmochim. Acta 224, 276–281.

Greenwood, R.C., Barrat, J.-A., Scott, E.R.D., Haack, H., Buchanan, P.C., Franchi, I.A., Yamaguchi, A., Johnson, D., Bevan, A.W.R., Burbine, T.H., 2015. Geochemistry and oxygen isotope composition of main-group pallasites and olivine-rich clasts in mesosiderites: implications for the "Great Dunite Shortage" and HED-mesosiderite connection. Geochim. Cosmochim. Acta 169, 115–136.

Hellmann, J.L., Kruijer, T.S., Van Orman, J.A., Metzler, K., Kleine, T., 2019. Hf-W chronology of ordinary chondrites. Geochim. Cosmochim. Acta 258, 290–309.

Hilton, C.D., Bermingham, K.R., Walker, R.J., McCoy, T.J., 2019. Genetics, crystallization sequence, and age of the South Byron Trio iron meteorites: new insights to carbonaceous chondrite (CC) type parent bodies. Geochim. Cosmochim. Acta 251, 217–228.

Hilton, C.D., Walker, R.J., 2020. New implications for the origin of the IAB main group iron meteorites and the isotopic evolution of the noncarbonaceous (NC) reservoir. Earth Planet. Sci. Lett. 540, 116248.

Hopp, T., Budde, G., Kleine, T., 2020. Heterogeneous accretion of Earth inferred from Mo-Ru isotope systematics. Earth Planet. Sci. Lett. 534, 116065.

Hunt, A.C., Cook, D.L., Lichtenberg, T., Reger, P.M., Ek, M., Golabek, G.J., Schonbachler, M., 2018. Late metal-silicate separation on the IAB parent asteroid: constraints from combined W and Pt isotopes and thermal modelling. Earth Planet. Sci. Lett. 482, 490–500.

Johnson, B.C., Sori, M.M., Evans, A.J., 2020. Ferrovolcanism on metal worlds and the origin of pallasites. Nat. Astron. 4, 41–44.

Kleine, T., Hans, U., Irving, A.J., Bourdon, B., 2012. Chronology of the angrite parent body and implications for core formation in protoplanets. Geochim. Cosmochim. Acta 84, 186–203.

Kleine, T., Mezger, K., Munker, C., Palme, H., Bischoff, A., 2004. Hf-182-W-182 isotope systematics of chondrites, eucrites, and martian meteorites: chronology of core formation and early mantle differentiation in Vesta and Mars. Geochim. Cosmochim. Acta 68, 2935–2946.

Kleine, T., Walker, R.J., 2017. Tungsten isotopes in planets. Annu. Rev. Earth Planet. Sci. 45, 389–417.

Kruijer, T.S., Burkhardt, C., Budde, G., Kleine, T., 2017. Age of Jupiter inferred from the distinct genetics and formation times of meteorites. Proc. Natl. Acad. Sci. 114, 6712–6716.

Kruijer, T.S., Fischer-Gödde, M., Kleine, T., Sprung, P., Leya, I., Wieler, R., 2013. Neutron capture on Pt isotopes in iron meteorites and the Hf-W chronology of core formation in planetesimals. Earth Planet. Sci. Lett. 361, 162–172.

Kruijer, T.S., Kleine, T., 2018. No ^{182}W excess in the Ontong Java Plateau source. Chem. Geol. 485, 24–31.

Kruijer, T.S., Kleine, T., 2019. Age and origin of IIE iron meteorites inferred from Hf-W chronology. Geochim. Cosmochim. Acta 262, 92–103.

Kruijer, T.S., Kleine, T., Borg, L.E., 2020. The great isotopic dichotomy of the early Solar System. Nat. Astron. 4, 32–40.

Kruijer, T.S., Kleine, T., Fischer-Gödde, M., Burkhardt, C., Wieler, R., 2014a. Nucleosynthetic W isotope anomalies and the Hf-W chronometry of Ca-Al-rich inclusions. Earth Planet. Sci. Lett. 403, 317–327.

Kruijer, T.S., Touboul, M., Fischer-Gödde, M., Bermingham, K.R., Walker, R.J., Kleine, T., 2014b. Protracted core formation and rapid accretion of protoplanets. Science 344, 1150–1154.

Kruijer, T.S., Sprung, P., Kleine, T., Leya, I., Burkhardt, C., Wieler, R., 2012. Hf-W chronometry of core formation in planetesimals inferred from weakly irradiated iron meteorites. Geochim. Cosmochim. Acta 99, 287–304.

Lugmair, G.W., Shukolyukov, A., 1998. Early solar system timescales according to ^{53}Mn-^{53}Cr systematics. Geochim. Cosmochim. Acta 62, 2863–2886.

Matthes, M., van Orman, J.A., Kleine, T., 2020. Closure temperature of the Pd-Ag system and the crystallization and cooling history of IIIAB iron meteorites. Geochim. Cosmochim. Acta 285, 193–206.

Nichols, C.I.O., Bryson, J.F.J., Herrero-Albillos, J., Kronast, F., Nimmo, F., Harrison, R.J., 2016. Pallasite paleomagnetism: quiescence of a core dynamo. Earth Planet. Sci. Lett. 441, 103–112.

Poole, G.M., Rehkämper, M., Coles, B.J., Goldberg, T., Smith, C.L., 2017. Nucleosynthetic molybdenum isotope anomalies in iron meteorites – new evidence for thermal processing of solar nebula material. Earth Planet. Sci. Lett. 473, 215–226.

Qin, L.P., Dauphas, N., Wadhwa, M., Markowski, A., Gallino, R., Janney, P.E., Bouman, C., 2008. Tungsten nuclear anomalies in planetesimal cores. Astrophys. J. 674, 1234–1241.

Quitte, G., Birck, J.L., Allegre, C.J., 2005. Stony-iron meteorites: history of the metal phase according to tungsten isotopes. Geochim. Cosmochim. Acta 69, 1321–1332.

Rubin, A.E., 2018. Carbonaceous and noncarbonaceous iron meteorites: differences in chemical, physical, and collective properties. Meteorit. Planet. Sci. 53, 2357–2371.

Ruzicka, A., 2014. Silicate-bearing iron meteorites and their implications for the evolution of asteroidal parent bodies. Geochemistry 74, 3–48.

Scott, E.R.D., 1977. Pallasites—metal composition, classification and relationships with iron meteorites. Geochim. Cosmochim. Acta 41, 349–360.

Scott, E.R.D., Wasson, J.T., 1975. Classification and properties of iron meteorites. Rev. Geophys. 13, 527–546.

Spitzer, F., Burkhardt, C., Budde, G., Kruijer, T.S., Morbidelli, A., Kleine, T., 2020. Isotopic evolution of the inner solar system inferred from molybdenum isotopes in meteorites. Astrophys. J. 898, L2.

Spitzer, F., Burkhardt, C., Nimmo, F., Kleine, T., 2021. Nucleosynthetic Pt isotope anomalies and the Hf-W chronology of core formation in inner and outer solar system planetesimals. Earth Planet. Sci. Lett. 576, 117211.

Tarduno, J.A., Cottrell, R.D., Nimmo, F., Hopkins, J., Voronov, J., Erickson, A., Blackman, E., Scott, E.R.D., McKinley, R., 2012. Evidence for a dynamo in the Main Group Pallasite parent body. Science 338, 939.

Tornabene, H.A., Hilton, C.D., Bermingham, K.R., Ash, R.D., Walker, R.J., 2020. Genetics, age and crystallization history of group IIC iron meteorites. Geochim. Cosmochim. Acta 288, 36–50.

Touboul, M., Kleine, T., Bourdon, B., Van Orman, J.A., Maden, C., Zipfel, J., 2009. Hf–W thermochronometry: II. Accretion and thermal history of the acapulcoite–lodranite parent body. Earth Planet. Sci. Lett. 284, 168–178.

Touboul, M., Puchtel, I.S., Walker, R.J., 2015. Tungsten isotopic evidence for disproportional late accretion to the Earth and Moon. Nature 520, 530–533.

Walte, N.P., Solferino, G.F.D., Golabek, G.J., Silva Souza, D., Bouvier, A., 2020. Two-stage formation of pallasites and the evolution of their parent bodies revealed by deformation experiments. Earth Planet. Sci. Lett. 546, 116419.

Warren, P.H., 2011. Stable-isotopic anomalies and the accretionary assemblage of the Earth and Mars: a subordinate role for carbonaceous chondrites. Earth Planet. Sci. Lett. 311, 93–100.

Wasson, J.T., Choi, B.-G., 2003. Main-group pallasites: chemical composition, relationship to IIIAB irons, and origin. Geochim. Cosmochim. Acta 67, 3079–3096.

Willbold, M., Elliott, T., Moorbath, S., 2011. The tungsten isotopic composition of the Earth's mantle before the terminal bombardment. Nature 477, 195–198.

Wittig, N., Humayun, M., Brandon, A.D., Huang, S., Leya, I., 2013. Coupled W-Os-Pt isotope systematics in IVB iron meteorites: in situ neutron dosimetry for W isotope chronology. Earth Planet. Sci. Lett. 361, 152–161.

Wood, J.A., 1978. Pallasites and the growth of parent meteorite planets. In: LPS IX, pp. 1273–1275.

Worsham, E.A., Bermingham, K.R., Walker, R.J., 2017. Characterizing cosmochemical materials with genetic affinities to the Earth: genetic and chronological diversity within the IAB iron meteorite complex. Earth Planet. Sci. Lett. 467, 157–166.

Yang, J., Goldstein, J.I., 2006. Metallographic cooling rates of the IIIAB iron meteorites. Geochim. Cosmochim. Acta 70, 3197–3215.

Yang, J., Goldstein, J.I., Scott, E.R.D., 2010. Main-group pallasites: thermal history, relationship to IIIAB irons, and origin. Geochim. Cosmochim. Acta 74, 4471–4492.